33RD CONGRESS
OF THE INTERNATIONAL COUNCIL
OF THE AERONAUTICAL SCIENCES
STOCKHOLM, SWEDEN, 4-9 SEPTEMBER, 2022

ICAS 2022 SWEDEN

Optimization of installed compact and robust nacelles using surrogate models

Francisco Sánchez-Moreno[1*], David MacManus[1], Josep Hueso-Rebassa[1], Fernando Tejero[1], Christopher Sheaf[2]

[1]Centre for Propulsion and Thermal Power Engineering, School of Aerospace, Transport and Manufacturing, Cranfield University, Bedfordshire, MK43 0AL, United Kingdom
[2]Rolls Royce Plc., P.O. box 31, Derby, DE24 8BJ, United Kingdom

*Corresponding author: fran.sanchez-moreno@cranfield.ac.uk

Abstract

The design and optimization of aero-engine nacelles in a configuration installed on the airframe may be an important consideration to realize the cycle benefits of new ultra-high bypass ratio aero-engines. However, this is typically a high-dimensional design problem and there is a need to reduce the associated computational costs. This work presents a method for aerodynamic nacelle optimization for an installed configuration and provides further knowledge about the characteristics of this design space. The methodology includes single fidelity surrogate models built with inviscid flow solutions. Gaussian process regression and artificial neural networks are tested as modelling techniques. Viscous computations are used to assess the optimized designs at cruise and off-design windmilling diversion condition. This approach yielded an optimal design with a reduction in fuel burn of about 0.56% relative to a design optimized in isolated configuration without considering the powerplant integration effects. The optimal design also met the robustness criteria in terms of limited flow separation at the windmilling diversion conditions.

Keywords: nacelle, optimization, installation effects, surrogate model, CFD

1. Introduction

Reduction of fuel burn is a key consideration in commercial aviation. Within this context, there has been an increase in the bypass ratio (BPR) of turbofan aero-engines to reduce the specific thrust and to increase the propulsive efficiency [1]. However, the expected associated larger fan diameter may incur an additional overall drag and weight penalty for the aircraft [2]. Moreover, the integration and interference effects of the aero-engine with the airframe may become more significant. Consequently, it would be beneficial to develop compact nacelles that will not erode the benefit from the new engine cycles. Although traditional nacelle design approaches have focused on minimizing the drag in isolated configuration [3,4], these modern design technologies need to consider the design space of the aero-engine coupled with the airframe. The aerodynamic performance of the nacelle installed in the airframe can deviate substantially from the isolated case due to the aero-engine integration effects [2]. The major aerodynamic change is observed in the inboard side of the installed nacelle. Rudnik et al. [5] analyzed the integration aerodynamics for an Ultra High BPR-type of aero-engine with an A320-type airframe. It was concluded that an additional shock wave appears due to the installation which affects the rear part of the inboard nacelle and the pressure side of the wing. The intensity of the shock grows as the BPR increases. Hoheisel [6] estimated this increase in the drag due to the installation for a twin-engine aircraft of up to 50 drag counts which corresponds to about 15% of the aircraft total drag. The installation position also plays a key role in the overall system performance [7]. For close-coupled positions the adverse aerodynamic integration effects increase substantially [8] and the isolated benefit does not hold [9] which makes the installed nacelle design approach essential.

Aerodynamic shape design and optimization is a complex problem normally governed by a high number of design variables and non-linear flow physics. Surrogate modelling techniques have extensively been used in these problems to reduce the computational overhead [10-13]. Wang et al [14] applied a Kriging interpolation model built from viscous CFD data for the optimization of a rotor blade parameterized with 22 design variables. A complex optimal design with non-linear twist and variable chord length was obtained. Relative to a baseline design, a significant weakening in the blade-tip vortex was obtained with an increase in the blade efficiency of 3.4%. In the same line, artificial neural networks (ANN) technique has also been proven to efficiently model the non-linear aerodynamic behavior [15,16]. Zuccolo et al. [17] compared the modelling ability of a Kriging and an ANN surrogate model for the prediction of aerodynamic characteristics of exhaust afterbodies. RANS CFD data was used for a range of Mach numbers from 0.6 to 1.4. A better modelling performance was obtained for the ANN model with uncertainties in the afterbody drag for a 2σ confidence interval of ±0.01 and ±0.013 for the ANN and Kriging models respectively. However, there is a dearth of literature within the context of installed nacelle aerodynamic shape optimization. Tejero et al. [18] presented a method to consider the integration effects within the nacelle optimization process. The methodology considered both active subspaces as dimensionality reduction technique and co-Kriging as a surrogate model. The design space was explored using a Euler computational fluid dynamics (CFD) model as Reynolds-Averaged Navier-Stokes (RANS) models become computationally prohibitive for this high dimensional problem. Historically, inviscid CFD models have commonly been used for powerplant integration assessments as they have been proven to capture the main aerodynamic interference aspects [19,20]. In the multi-fidelity co-Kriging model, the inviscid data is combined with few expensive RANS datapoints. As a result, an optimized nacelle design was obtained that provided a reduction in the fuel burn of approximately 0.65%.

An additional challenge in nacelle design lies with the different flow conditions that arise throughout the aircraft mission. Consequently, not only cruise but also off-design windmilling conditions have to be considered [4,21]. This is even more significant for compact nacelles that are expected for the next generation of Ultra-High BPR aero-engines [4,21]. The reason is that as the nacelle becomes more compact the curvature gradients along the nacelle are higher and therefore the aerodynamic sensitivity to off-design conditions increases.

This paper presents a methodology for compact and aerodynamically robust nacelle optimization for an installed configuration using a single fidelity surrogate modelling approach based on Euler computations. Kriging interpolation and ANN are used as low-order models. The novelty of the paper is in the use of ANN as surrogate modeling technique for nacelle optimization and the consideration of robustness to off-design conditions within a nacelle optimization process for an installed configuration.

2. Methodology

The proposed optimisation method is based on the cruise condition with a subsequent assessment of the optimised design at windmilling diversion condition to ensure the aerodynamic robustness of the design (Table 1). This robustness assessment at windmilling diversion conditions is based on a flow separation criterion with a limit of 10% of the nacelle length. Good aerodynamic performance under windmilling diversion conditions are needed for a sufficient range under extended range twin engine operational performance standards (ETOPS) [22].

	Mach number	MFCR	$C_{L\text{-}Trim}$
Cruise	0.85	0.7	0.5
Windmilling diversion	0.65	<0.5	0.44

Table 1 – Definition of each operating condition considered in the optimization method.

2.1 Geometry definition

The installed nacelle geometry is parameterized through intuitive class shape transformations (iCSTs) [23]. The iCSTs control 8 different azimuthal aero-lines of the nacelle (Figure 1a). As this work is focused on a compact nacelle architecture given by L_{nac}/r_{hi} = 3.1 and r_{te}/r_{hi} = 0.95, 4 intuitive variables per aero-line are changed in the design process: r_{if}, r_{max}, f_{max} and β_{nac} (Figure 1b). The full installed nacelle geometry is defined by 32 variables. However, from a computational cost point of view the dimensionality of the problem has to be reduced. In the proposed methodology, 3 aero-lines in the inboard side of the nacelle are selected (ψ = 45º, 90º and 135º, Figure 1a). The reason is that the aero-engine aerodynamic integration effects primarily affect the inboard part of the nacelle. The outboard side is maintained from a baseline design which was obtained through a nacelle optimization process for an isolated configuration using the method developed by Tejero et al. [3]. This design has inboard-outboard symmetry and is used as reference in the present work relative to which the benefits are reported. The method used to design the nacelle in isolation is based on a multi-point optimization approach that considers operating conditions both in the cruise segment and at off-design windmilling conditions. A CFD-in-the-loop technique driven by a genetic algorithm is applied with about 5000 3D RANS calculations per optimization. This baseline design is robust for off-design windmilling conditions which is a key aspect for compact nacelle architectures [21]. The windmilling diversion condition is characterized by a very low mass flow capture ratio (MFCR) and the initial forebody radius at the nacelle leading edge (r_{if}) becomes the key parameter to control flow separation over the nacelle forebody. Therefore, r_{if} is kept constant as per the reference design in every aero-line to enable acceptable aerodynamics at windmilling diversion conditions. Overall, 9 design variables control the degrees of freedom for the installed nacelle design (Figure 1). Fixed intake offset and scarf angle are also considered to improve the aerodynamic performance of the nacelle at incidence (Figure 1b) [24]. A detailed description of the nacelle parameterisation through iCST was provided by Tejero et al. [25].

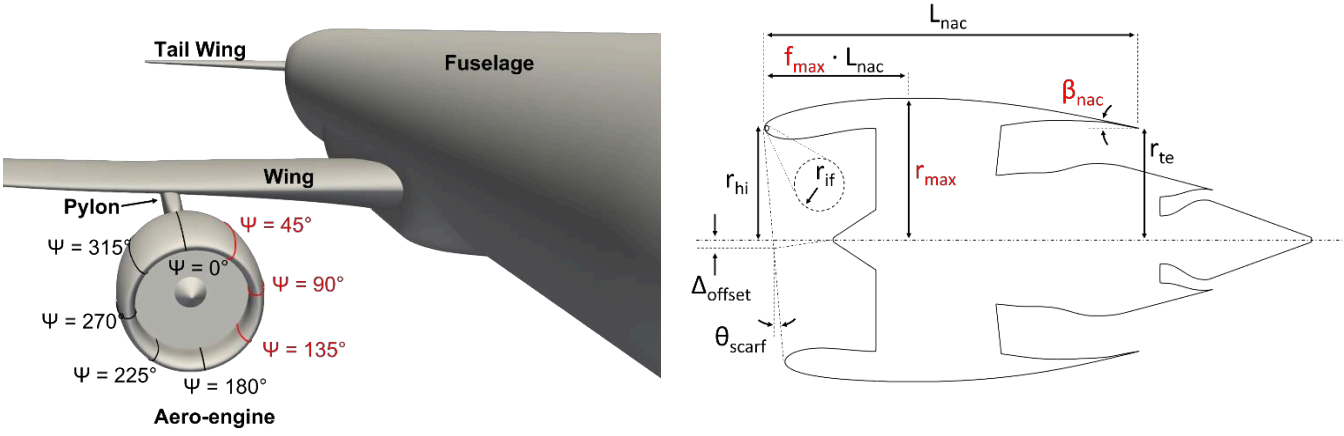

a) Azimuthal aero-lines b) Parameterisation of a 2D aero-line

Figure 1 - Installed nacelle parameterization. Aero-lines and parameters marked in red are the design variables of the proposed design method.

The full aero-engine configuration is generated by combining the nacelle design with a representative intake [26] and separate jet exhaust [27] which have been designed to alleviate adverse flow features across the investigated design space. The resulting powerplant is representative of an Ultra-High BPR configuration with a standard net thrust (F_N) of approximately 60kN [27]. The propulsion system is integrated in the airframe through a representative pylon [28]. The NASA common research model (CRM) is used as the airframe as it is representative of a wide-body twin-engine commercial transport aircraft [29]. The installation position is defined by the axial (dx) and vertical (dz) offset between the wing leading edge and the nacelle top line trailing edge [28,9]. An expected installation position for future civil aero-engines is considered: dx/C_{wing} = 0 and dz/C_{wing} = 0.1, where C_{wing} is the local wing chord. In common with the CRM throughflow configuration, the powerplant is installed at 33.4% of

the semi-span wing length from the fuselage mean axis with a pitch-up and toe-in angles of 1.75º and 2.25º, respectively [29].

2.2 Numerical method

Two CFD fidelities are used in this work to accelerate the design process. The low-fidelity model solves the compressible and inviscid flow governed by the Euler equations through a pressure-based solver [30]. This model is used to understand the design space and to generate a database to build the surrogate models. The higher-fidelity model solves the viscous and compressible flow governed by the Reynolds-Averaged Navier-Stokes equations through an implicit and density-based solver [30]. The RANS model is used to provide the final evaluation of the down selected optimal designs both at cruise and windmilling diversion condition. In the RANS CFD model, turbulence closure is achieved by the k-ω SST model [31]. Upwind second order spatial discretization and Green-Gauss node-base scheme are used in both models.

A hemispherical domain with half of the aircraft configuration is used due to the left-right symmetry of the model and helps to reduce the computational overhead. From the 4th AIAA Drag Prediction Workshop [32], the radius of the hemispheric domain is set to 100 times the local wing chord at the installation spanwise location. The domain is discretized using a hybrid meshing strategy composed of prism layers in the boundary layer and tetrahedral elements far from the walls. In the RANS model, a y^+ below 1 is ensured in every surface to resolve the boundary layer, which results into an overall cell count of 115 million elements. The model validation and mesh independence studies were conducted by Goulos et al [28]. For the inviscid model, the overall mesh is coarsened by a factor of approximately 2 and the refinement in the boundary layer is removed. The total cell count reduces to about 20 million elements. The computational cost of the Euler-based model is reduced by a factor of about 30 relative to a RANS calculation which is a key aspect to enable an exploration of the design space.

The freestream conditions are imposed in the form of a pressure-farfield boundary condition in the farfield boundaries. Static temperature and pressure and flight Mach number are set. The fan face is modelleded by a pressure-outlet boundary condition with a target mass flow from the corresponding operating condition. A pressure intlet boundary condition is set both in the core and bypass exhaust inlet boundaries. Total pressure and temperature are specified from the prescribed engine cycle. The model symmetry plane is modeled with a symmetry boundary conditon. Finally, slip and non-slip wall conditions are imposed in the remainding model boundaries for the Euler and RANS calculations respectively.

2.3 Thrust and drag accounting system

The overall performance of full aircraft system is evaluated through a Thrust-Drag Accounting method based on industrial standard practices [33] and extended to account for the pylon and airframe effects by Goulos et al. [28] (Figure 2). The forces are considered positive in the downstream direction. The streamtube-external forces define the drag domain and are represented by ϕ while the streamtube-internal forces correspond to the thrust domain and are expressed by θ. The gauge stream forces across the boundaries (F_G) are calculated by integrating the pressure and momentum terms over the area of interest and the exerted forces on the engine walls are computed by integrating the pressure and viscous terms. The Net Propulsive Force (NPF) (Eq. 1) is the metric used to quantify the overall engine performance and accounts for the aerodynamic balance between the thrust and drag domains. Whereas the thrust domain is represented by the Gross Propulsive Force (GPF) (Eq. 2) the drag domain is defined by the modified nacelle drag (D^*_{nac}) (Eq. 3). Similarly, the Net Vehicle Force (NVF) (Eq. 4) reports the overall aerodynamic performance of the combined airframe and powerplant system through the difference between the aero-engine NPF and airframe drag (D_{af}). NVF is the key metric which leads the nacelle optimisation method.

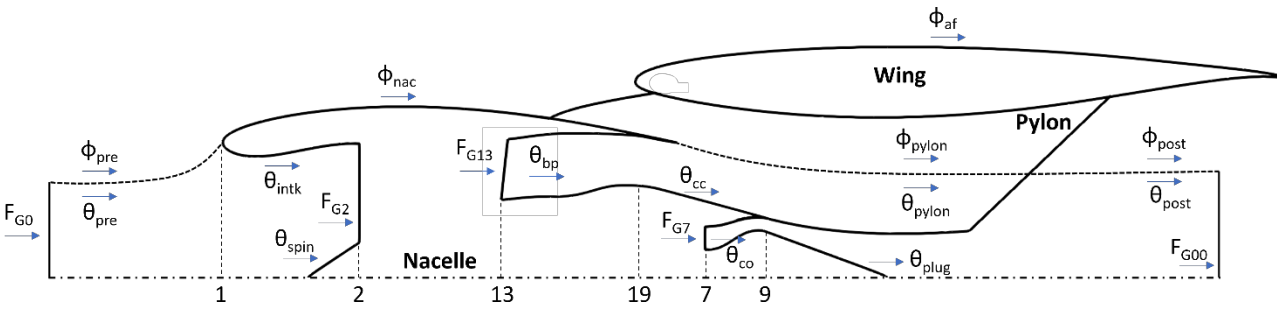

Figure 2 – Thrust and drag accounting method for the installed nacelle configuration.

$$NPF = GPF^* - F_{G0} - D^*_{nac} \tag{1}$$

$$GPF^* = F_{G13} + F_{G7} - \left(\theta_{bp} + \theta_{cc} + \theta_{co} + \theta_{plug} + \theta_{pylon}\right) \tag{2}$$

$$D^*_{nac} = \phi_{pre} + \phi_{nac} \tag{3}$$

$$NVF = NPF - D_{af} \tag{4}$$

2.4 Surrogate modelling techniques

The transonic aerodynamics of compact nacelles is highly non-linear. Kriging interpolation and artificial neural networks are used in this work due to their ability to handle non-linear characteristics.

2.4.1 Gaussian process regression (Kriging)

The Gaussian process regression, or Kriging method, is used to create single-fidelity surrogate models [34]. A surrogate model based on Kriging approximates the value of a function $y(x)$ by a linear combination of a regression $\mu(x)$ and a correlation functions $z(x)$ (Eq. 5).

$$\hat{y}(x) = \mu(x) + z(x) \tag{5}$$

The regression function is a linear combination of p polynomials of order $0 \leq p \leq 2$, where $\beta = (\beta_0, \ldots\beta_k, \ldots\beta_p)$ corresponds to a vector of regression coefficients (Eq. 6). The parameter p defines the order of the regression function which can be constant ($p = 0$), linear ($p = 1$) or quadratic ($p = 2$). If a constant regression model is used, the function will have $p = 1$ and $f_k = 1$ [34,17].

The correlation function $z(x)$ has the form of a stochastic process of Gaussian distributions with zero mean and standard deviation σ (Eq. 7) [17]. It is a combination of one-dimensional correlations that are functions of the position between a point x relative to the rest of the points of the dataset N. γi are weighting coefficients, Rj is one of the dim NxN correlation matrices where dim is the dimensionality of the problem, $wij - xij$ relates to the distances between points in the dataset and θ is the correlation parameter between input samples. $r(\theta, (wij - xj)$ is a column vector that accounts for the distances between the target point x to all other input points. The correlation matrix of the dataset is approximated by correlation functions. Different correlation functions such as absolute exponential, squared exponential, cubic and linear functions are considered within this work to find the best fit of the model (Table 2).

$$\mu(x) = \sum_{k=0}^{p} \beta_k f_k(x) \tag{6}$$

$$z(x) = \sum_{i=1}^{N} \Upsilon_i \prod_{j=1}^{dim} f\left(R_j\left(\theta, \left(w_{ij} - x_{ij}\right)\right), r\left(\theta, \left(w_{ij} - x_j\right)\right)\right) \tag{7}$$

The correlation matrix contains 1.0 on its diagonal as it represents the correlation of one point with itself. This forces the prediction model to pass exactly through the input data points and may cause

overfitting for problems where the input data has some amount of noise. This issue can be addressed with the addition of a controlled uncertainty parameter to the diagonal of the matrix that allows the surrogate model to float around the training points. This parameter is called a nugget (ϵ). The selection of regression and correlation functions, as well as nugget is problem dependent and it is studied in this work to the design space of installed nacelles. To use Kriging as a prediction model for unknown data points, it first needs to be trained. The training step of the model consists of the determination of the hyperparameters of the Kriging model and this is done through the maximization of the likelihood function [34].

Correlation function	$\boldsymbol{R_j\left(\theta,(w_{ij}-x_{ij})\right)}$
Absolute exponential	$e^{-\theta\lvert w_j-x_j\rvert}$
Squared exponential	$e^{-\theta(w_j-x_j)^2}$
Cubic	$1-3\varepsilon^2+2\varepsilon^3, \varepsilon=\min\left(1,\theta\lvert w_j-x_j\rvert\right)$
Linear	$max\left(0,1-\theta\lvert w_j-x_j\rvert\right)$

Table 2 – Correlation functions considered for the Kriging surrogate model.

2.4.2 Artificial neural network

An artificial neural network is a parallel computational model that imitates the processing behaviour of the human brain [35]. The elemental unit of an ANN is called a neuron. The layout of an ANN is composed of a set of neurons divided into layers which are interconnected (Figure 3a). There are three types of layers: input layer, hidden layers and output layer (Figure 3a) [36]. The hidden layers are the main processing elements of an ANN and the number of them depends on the complexity of the system to be modelled. There are two types of networks: (a) feed-forward networks and (b) recurrent networks. While in a feed-forward ANN the signal goes from inputs to outputs, back propagation loops of information between the different layers is enabled in recurrent ANN. The higher complexity of recurrent networks makes them more capable to model complex physics. However, the current learning algorithms of these networks are limited. In this work, feed-forward multi-layer perceptron (MLP) type of ANN are used.

The mathematical model of an ANN is based on a linear combination of weighting coefficients between neurons (Eq. 8). The output of a neuron y_k is the result of the sum of the weighted inputs to the neuron k plus a bias term b_k which is used to improve the fitting of the modelling data (Figure 3b). The weighted inputs are evaluated as the product between the input signal from every j neuron x_j in the previous layer and the corresponding weighting coefficient w_{kj}. Additionally, an activation function φ to limit the neuron output is applied which helps in the learning process of the NN (Eq. 8) (Figure 3b). The choice of the activation function is highly problem dependant and is selected as part of a hyperparameters sensitivity analysis. In this work, ReLu, Sigmoid and Hyperbolic tangent are considered (Table 3).

$$y_k = \varphi(v_k) = \varphi\left(\sum_{j=1}^{m} w_{kj}\, x_j + b_k\right) \tag{8}$$

Activation function	$\boldsymbol{\varphi(v_k)}$
ReLu	$max(0,v_k)$
Sigmoid	$(1+e^{-v_k})^{-1}$
Hyperbolic tangent	$\tanh(v_k)$

Table 3 – Activation functions considered for the ANN surrogate model.

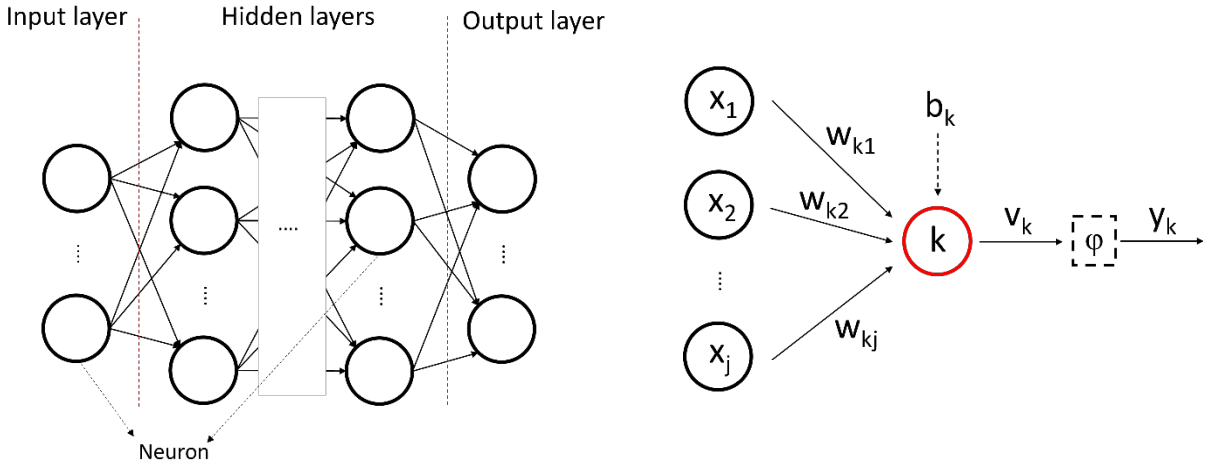

a) Generic layout of a neural network b) Mathematical model of a neuron *k*

Figure 3 – Artificial neural network model.

In the training process of a neural network the weights and biases are adjusted so a cost function is minimized [37]. In this work, the absolute root mean squared error (RMSE) cost function is used based on NVF (Eq. 9). The widely used gradient descent algorithm called ADAM is used due to its fast convergence and ability to handle large datasets [38]. L2 norm regularization factors are used to avoid overfitting in the model.

$$RMSE_{NVF} = \sqrt{\frac{1}{N}\sum_{i}(NVF_{CFD} - \mathrm{NVF}_{model})^2} \tag{9}$$

3. Results

3.1 Design space exploration

A design space exploration (DSE) at the cruise condition was conducted using the inviscid flow solver to understand the relationship between the different performance metrics (Section 2.3) and the design variables. A key consideration to suficiently populate the design space is the ratio between the number of samples in the DSE ($N_{samples}$) and the degrees of freedom of the design problem (N_{DOF}). In this case $N_{samples}/N_{DOF}$ = 80 was used to provide an DSE of 720 designs. The Latin Hypercube Sampling (LHS) technique was used.

The DSE highlights trade-offs between the NPF and D_{af} components of the overall NVF (Eq. 4) (Figure 4a). The optimal design space for maximum NVF benefits within this DSE is located at the regions of NPF benefits but with some D_{af} penalties (Figure 4). NPF is decomposed into its constituent metrics to understand the impact of the nacelle drag and the thrust (Eq. 1). The designs with the maximum NVF benefits are located in the zone of D^*_{nac} benefits and GPF* penalties (Figure 4b). This highlights the general opposing effects of the nacelle geometry changes on the nacelle and airframe aerodynamics. The best design from this DSE has an inviscid NVF benefit relative to the baseline of $\Delta NVF/F_N$ = 0.75%. This NVF benefit comes from the balance between $\Delta D_{af}/F_N$ = -1.55%, $\Delta D^*_{nac}/F_N$ = 3.20% and $\Delta GPF^*/F_N$ = -0.90%. Athough there is a penalty in airframe drag and gross propulsive force of the engine, the benefit achieved in the reduction of the nacelle drag is more beneficial and the overall system NVF is improve. The CFD assessment consider a retrimming to C_L = 0.5 as per the CRM cruise condition [29] to account for the changes in lift.

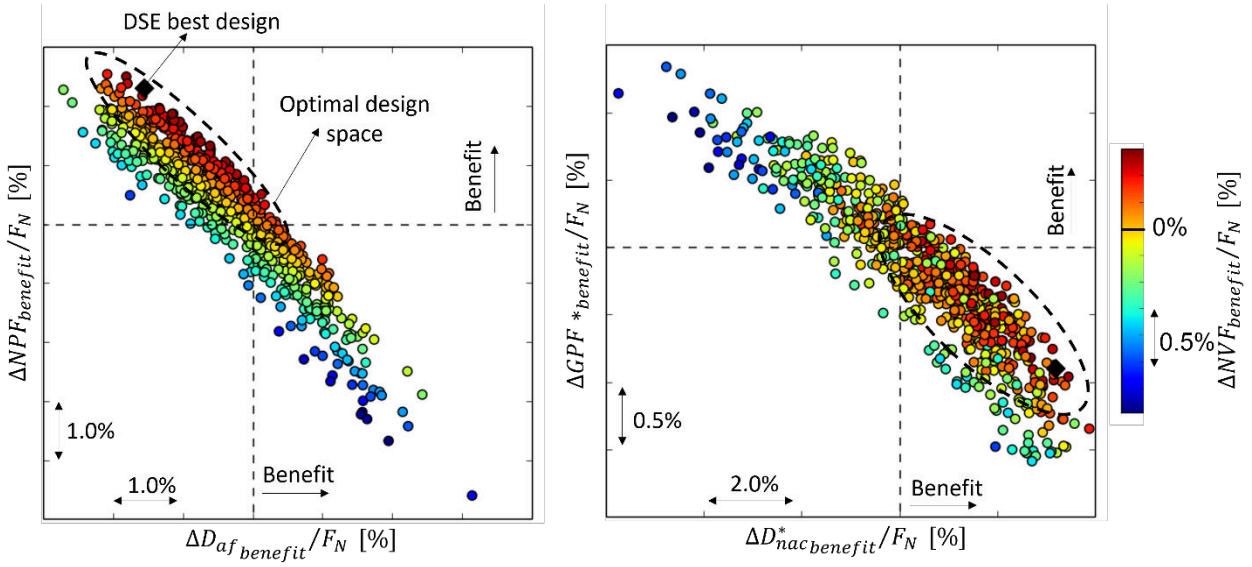

a) NPF benefit against D_{af} benefit b) D^*_{nac} benefit against GPF* benefit

Figure 4 – Design space from the Euler DSE coloured by NVF benefit.

There is an interest in understanding the relationship between the different design variables with the key metric NVF. The whole NVF range is split into different subranges of NVF benefit to identify the region of the optimal design space for each design variable (Figure 5). There is not a clear trend of the β_{nac} at every aero-line of the inboard part of the nacelle with the NVF. It can be concluded that f_{max} and r_{max} are the dominant variables from a NVF optimization point of view for the design method proposed. In particular, there is a clear trend for $r_{max,45}$ and f_{max} for all aero-lines to low values and $r_{max,90}$ to high values of the considered design space. $r_{max,135}$ stays around the middle of the analyzed design space.

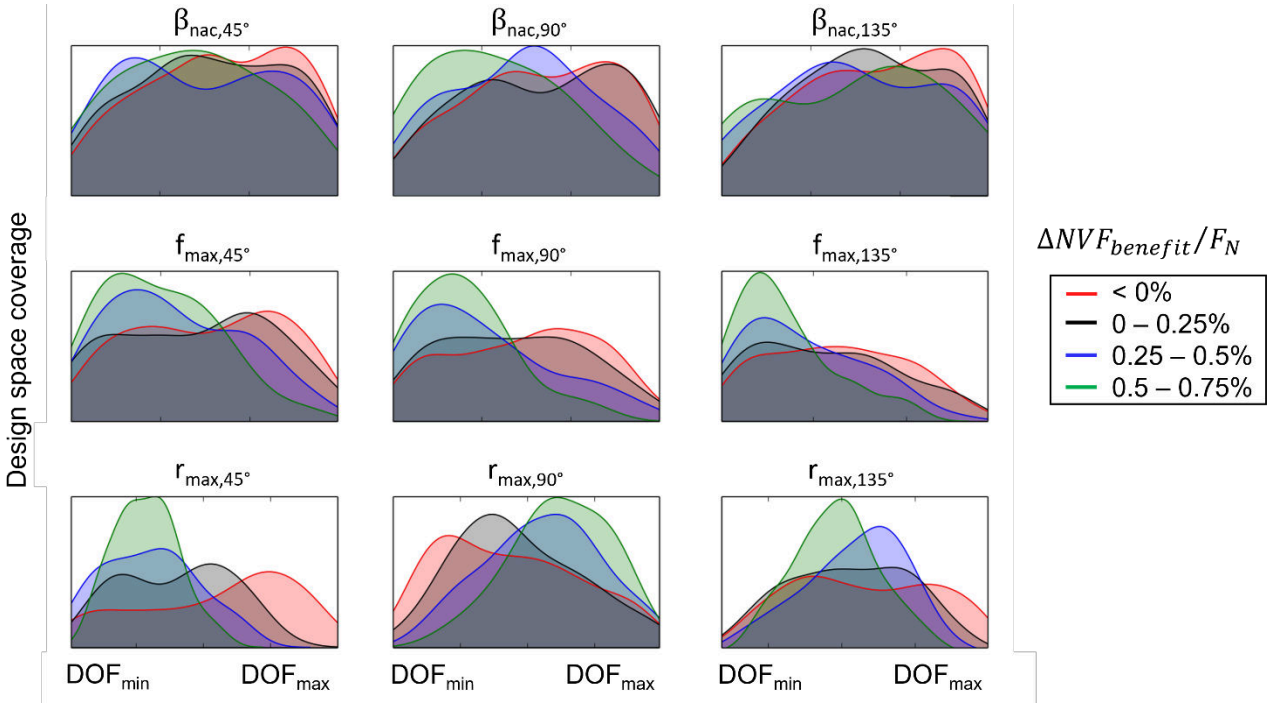

Figure 5 – Impact of the design variables on the NVF benefit.

3.2 Construction of the surrogate models

Both the Kriging and the ANN surrogate models have been built through an optimization process of the different hyperparameters of the model. This requires an independent validation dataset used to evaluate the predicting performance of each surrogate model built. An addition LHS for a ratio of $N_{samples}/N_{DOF} = 20$ has been used for this purpose. The minimization of the $RMSE_{NVF}$ (Eq. 9) has been used to optimize the surrogate model fitting.

For the Kriging model four correlation function have been considered: absolute exponential, squared exponential, cubic and linear. Additionally, constant, linear and quadratic regression function have been tested. The nugget factor has been variated from $1e^{-5}$ to $1e^{-9}$. The highest modelling performance has been found for the absolute exponential correlation function, the quadratic regression function and a nugget value of $1e^{-7}$ (Figure 6a). The cross-validation based on NVF of the selected model with the CFD independent dataset yields a $RMSE_{NVF}$ of 0.117% of the standard net thrust (F_N) (Figure 6b).

The optimization of the ANN model considers three activation functions: ReLu, sigmoid and hyperbolic tangent. For each activation function different networks architectures have been built. The number of hidden layers has been varied from 10 to 22. The neurons number per layer ranged from 20 to 320. The L2 norm regularization factors have been changed from 10^{-3} to 10^{-6}. The optimal ANN model has been found for a $RMSE_{NVF}$ of 0.124% of the standard net thrust for a combination of ReLu activation function, 13 hidden layers with 320 neurons and 10^{-4} as regularization factors (Figure 7).

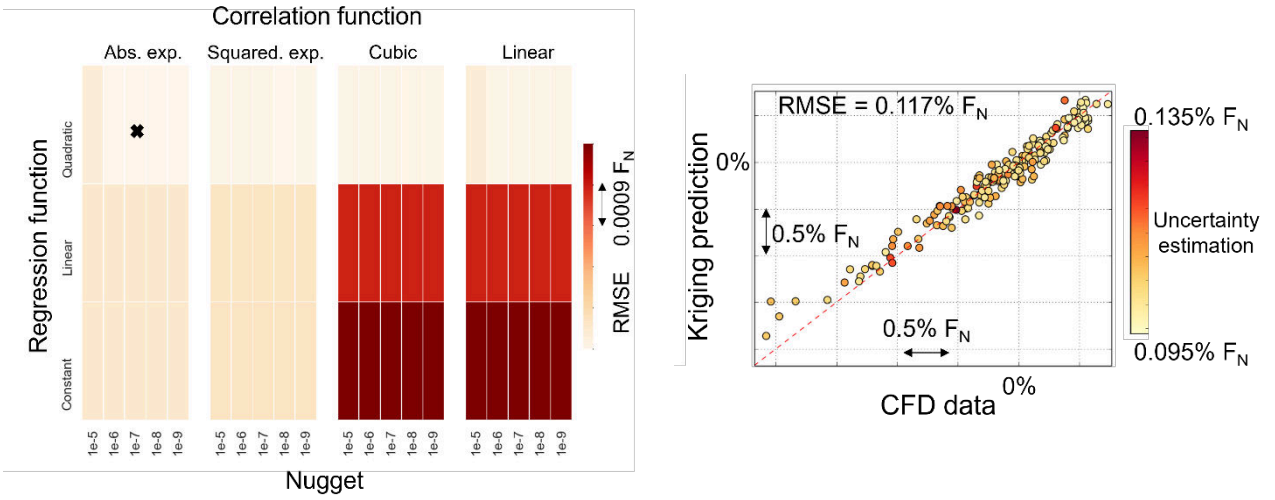

a) Hyperparameters optimization for the Kriging surrogate model.

b) Cross-validation based on NVF of the selected Kriging surrogate model.

Figure 6 – Kriging surrogate model.

Overall, similar modelling performance for ΔNVF prediction have been found for both the Kriging and the ANN models based on the $RMSE_{NVF}$ as a global measure unit of uncertainty. Additionally, the models have been interrogated in the analyzed design space to test their response against the trends of the CFD-based design space. A 1-dimensional interrogation for each design variable has been performed by keeping the rest of the parameters fixed to the baseline nacelle design (Section 2.1). The same trend for each variable is found not only between the Kriging and the ANN models but also with the CFD-based design space exploration results (Figure 5, Figure 8). As stated before, the impact of β_{nac} is neglectable in comparison with f_{max} and r_{max}. The capability of the Kriging technique to estimate the uncertainty in the prediction shows that this is maximum in the bounds of the design space as could be expected.

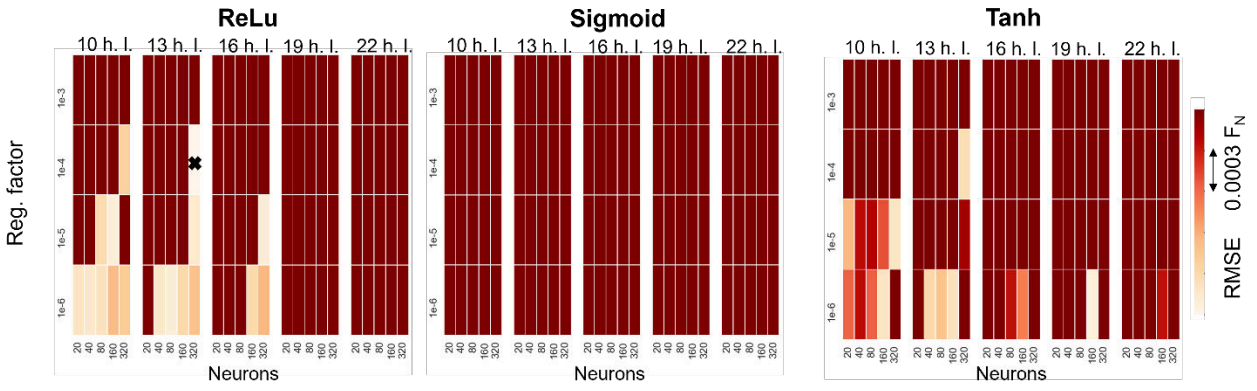

a) Hyperparameters optimization for the ANN surrogate model.

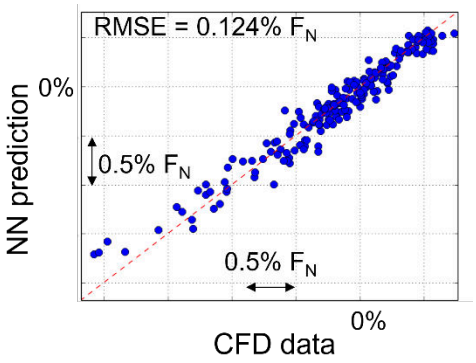

b) Cross-validation based on NVF of the selected ANN surrogate model.

Figure 7 – ANN surrogate model.

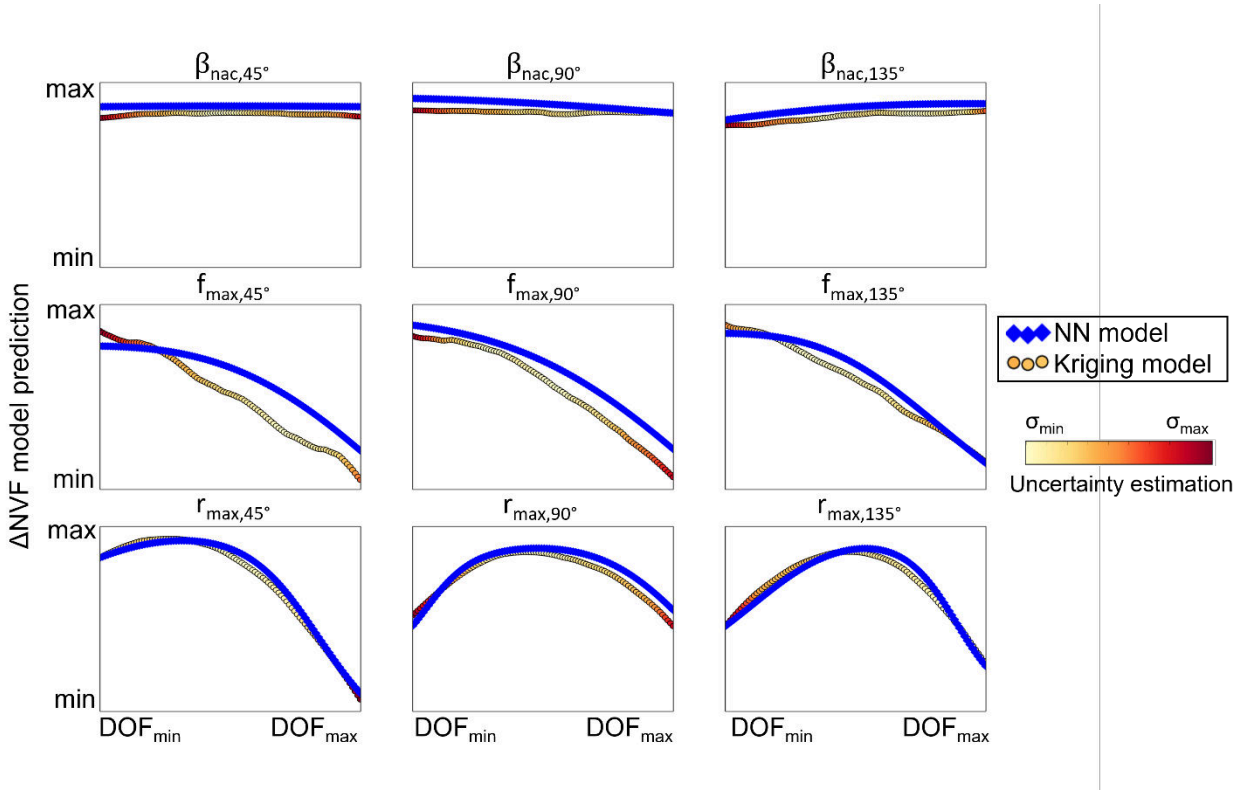

Figure 8 – 1-dimensional interrogation of the Kriging and ANN surrogate models in the analysed design space.

3.3 Surrogate-based installed nacelle optimization

To perform the surrogate-based installed nacelle optimization, the NSGA-II genetic algorithm was coupled with the surrogate model. The objective is to maximize the cruise NVF benefit relative to the baseline design. The optimization was set up with a first generation of 300 samples to ensure a good

coverage of the design space. Subsequently, 100 additional generations with 50 samples per generation were considered to ensure the optimization convergence. This optimization approach has been verified for different benchmark cases. The computational cost associate to the optimization is almost negligible as the surrogate model evaluations are rapid.

Two independent optimizations were conducted, one with the Kriging and one with the ANN surrogate model. The optimal designs were evaluated with the inviscid CFD model to compare with the DSE results in the same currency. Relative to the baseline, the Kriging optimization found a design with a NVF benefit of 0.79% while the ANN yielded an optimal design with a NVF benefit of 0.63% (Figure 9a). While the ANN optimal design is below the DSE design with highest NVF benefit (0.75%), the Kriging one give a very slight improvement by 0.04% (Figure 9a). A RANS assessment of the Kriging optimal has been conducted to find the NVF benefit when the viscous terms are also included. The ANN optimum has not been evaluated as it is already underperforming the best design from the DSE. A RANS NVF benefit of 0.56% and 0.46% have been obtained for the Kriging optimum and DSE best designs respectively (Figure 9b). This 0.56% benefit in NVF equates to approximately 0.56% in fuel burn reduction. As concluded before, the 0.56% NVF improvement comes from a benefit in D^*_{nac} and a penalty in D_{af} and GPF* with reaches 2.30%, -1.04% and -0.70% respectively.

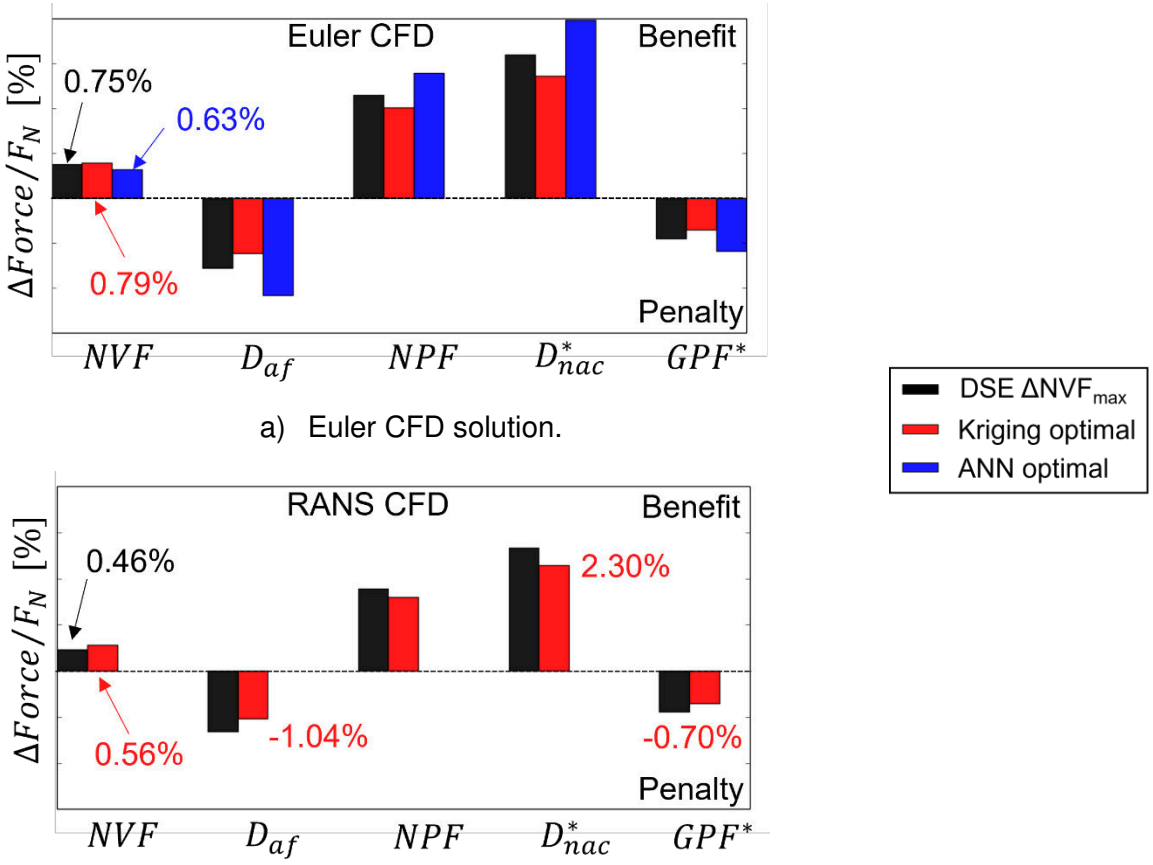

a) Euler CFD solution.

b) RANS CFD solution.

Figure 9 – Comparison of the performance metrics for the optimal designs

Both optimal designs and the DSE design with highest NVF follow the trends highlighted for the design variables at the optimal design space (Section 3.1) (Figure 10). The design optimized with the ANN surrogate model reaches the lower bounds of the considered design space for $r_{max,45}$, $f_{max,45}$, $f_{max,90}$, $f_{max,135}$ and $\beta_{nac,90}$ which might explain the reduced NVF benefit obtained. The comparison of the Kriging optimum and DSE best design in the dominant variables (f_{max} and r_{max}) shows small changes in most of the parameters. However, there is a notable difference in $f_{max,45}$ of the order of one third of the investigated design space span (Figure 10). However, for the high complexity of the design space of this problem both designs can be considered as very similar and the difference in $f_{max,45}$ may be balanced with small changes in other parameters to finally yield a similar NVF benefit.

The fact that the design with highest NVF from the DSE is already very similar to the optimized design indicates that the design space has been well populated in the DSE already. However, as both Kriging and ANN models are acceptable to model the design space, they could be used for trade studies or to apply geometrical constraints in the NVF optimization. This is pertinent as the design of a nacelle in installed configuration is a multi-disciplinary problem and structural or mechanical requirements might also have to be included.

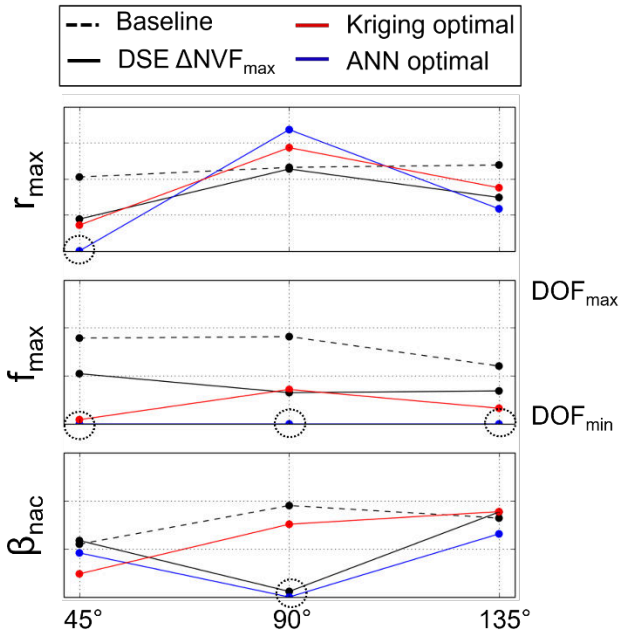

Figure 10 – Design variables for the optimal designs.

A comparison of the aerodynamics of the coupled engine-airframe configurations for the baseline and the optimized designs identifies the flow mechanisms that cause the overall NVF benefit. The reduction in $\Delta D^*_{nac}/F_N$ of 2.3% is essentially driving the NVF benefit. This drag reduction arises from an increase in the pressurization in the afterbody of the inboard nacelle caused primarily by an increase in the spatial separation between the wing and the nacelle (Figure 11). This affects the pressure distribution on the nacelle forebody with a more monotonic distribution, a higher forward nacelle loading, and ultimately a reduction in the nacelle drag (Figure 11). A concomitant effect appears in the pressure side of the wing that increases the static pressure on the forebody and causes a penalty in $\Delta D_{af}/F_N$ of -1.04% (Figure 11).

The aerodynamic robustness of the optimized nacelle under windmilling diversion conditions has been assessed through a comparison of the extents of the flow separation region based on the axial component of the wall shear stress. While the flow separation exhibited by the baseline design is L_{sep}/L_{nac} ~ 6.7%, the optimized nacelle separates to approximately 9.6% of the nacelle length (Figure 12). The optimal design is still valid as the 10% maximum limit has not been exceeded. However, this highlights the impact of other parameters besides r_{if} on the windmilling diversion separation. The reduction of f_{max} and r_{max} for a constant r_{if} increases the geometry curvature in the forebody and eventually the sensitivity to separation. This is what happens around the 45° aero-line of the optimized nacelle (Figure 10, Figure 12).

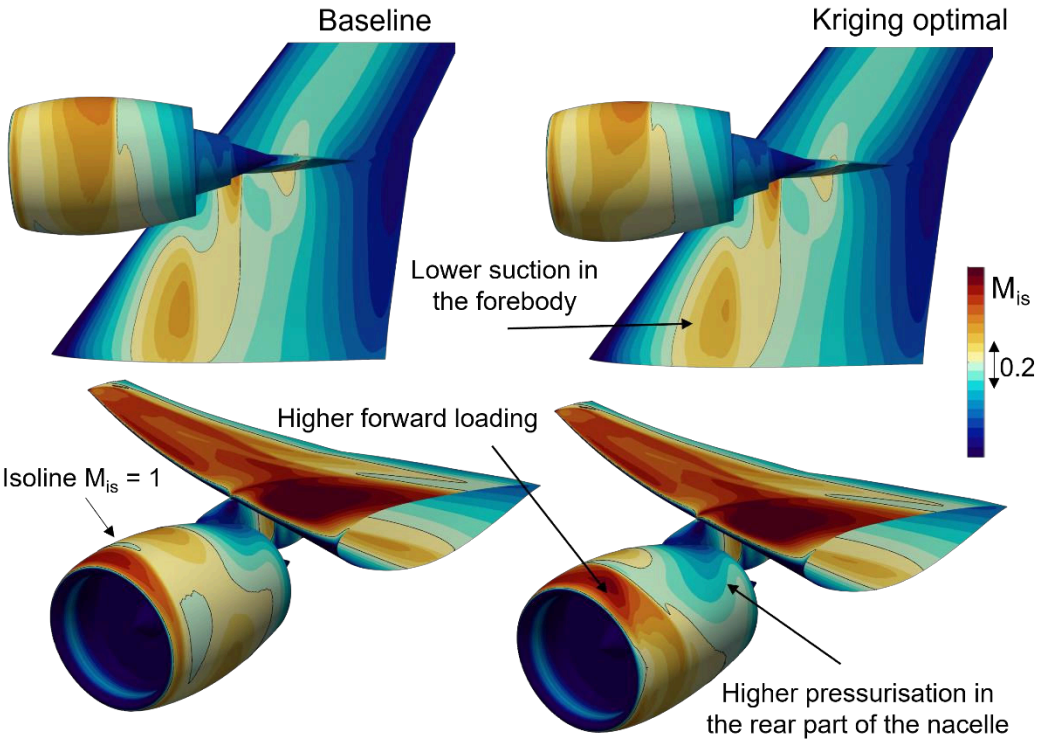

Figure 11 – Isentropic Mach number distributions for the baseline and the optimised design with the Kriging surrogate model.

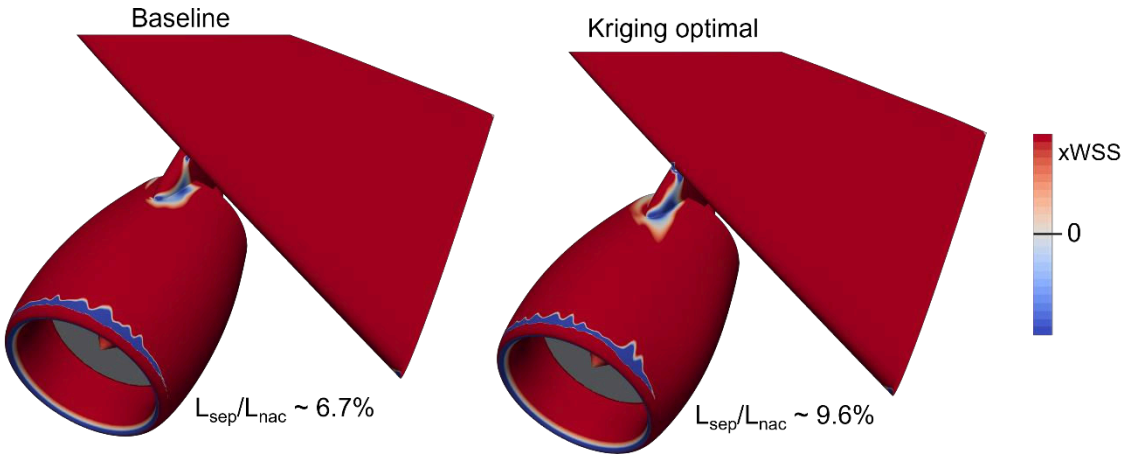

Figure 12 – Contours of axial wall shear stress to show the flow separation extent at windmilling diversion for the baseline and the optimised design with the Kriging surrogate model.

4. Conclusions

This paper has presented a method for nacelle optimization in a configuration installed on the airframe. The methodology combines a surrogate modelling technique with inviscid flow solutions to drive an optimization algorithm. A posteriori viscous CFD assessment of the optimized design is conducted. The approach has yielded an optimal design with a fuel burn reduction of approximately 0.56% relative to a baseline design optimized in isolation. This highlights the benefits of considering the integration effects within the nacelle design process. The aerodynamic robustness to off-design flow conditions has been considered in the proposed methodology. The optimized installed design has been evaluated for the windmilling diversion condition and meets the criterion on local flow

separation. Additionally, acceptable modelling performance have been proven for the Kriging and the neural network surrogate models which could be used for trade studies or to impose geometrical constraints in the optimization process.

5. Acknowledgment

This project has received funding from the Clean Sky 2 Joint Undertaking under the European Union's Horizon 2020 Research and Innovation Program under Grant Agreement No 820997.

6. Copyright Statement

References

[1] Daly M. *Jane's aero-engines*. 28th ed. Surrey: HIS Global Ltd, 2010, p.64.

[2] Daggett DL, Brown ST and Kawai RT. Ultra-efficient engine diameter study. Report 2003-212309, NASA Contract Report, 2003.

[3] Tejero F, Robinson M, MacManus DG and Sheaf C. Multi-objective optimisation of short nacelles for high bypass ratio engines. *Aerospace Science and Technology*, Vol. 91, pp 410-421, 2019.

[4] Tejero F, MacManus DG, Matesanz-Garcia J, Swarthout A and Sheaf CT. Towards the design and optimisation of future compact aero-engines: intake/fancowl trade-off investigation. *56th 3AF International Conference*, Toulouse, France, 28-30 March 2022.

[5] Rudnik R, Rossow CC and Geyr HFV. Numerical simulation of engine/airframe integration for high-bypass engines. *Aerospace Science and Technology*, Vol. 6, pp 31-42, 2002.

[6] Hoheisel H. Aerodynamic aspects of engine-aircraft integration of transport aircraft. *Aerospace Science and Technology*, Vol. 7, pp 475-487, 1997.

[7] Sibilli T, Savill M, Sethi V, MacManus D and Rolt A. Numerical simulation of propulsion system integration for very high bypass ratio engines. *Proceedings of ASME Turbo Expo*, Copenhagen, Denmark, 11-15 June 2012, GT2012-68908.

[8] Ingraldi AM, Kariya TT, Re RJ, Pendergraft Jr OC. Interference effects of very high bypass ratio nacelle installations on a low-wing transport. *Journal of Engineering for Gas Turbines and Power*, Vol. 114, pp 809-815, 1992.

[9] Tejero F, Goulos I, MacManus DG and Sheaf C. Effects of aircraft integration on compact nacelle aerodynamics. *AIAA SciTech Forum*, Orlando, USA, 6-10 January 2020, AIAA2020-2225.

[10] Song C, Song W and Yang X. Gradient-enhanced hierarchical kriging model for aerodynamic design optimization. *Journal of Aerospace Engineering*, Vol. 30, No. 6, 2017.

[11] Heidebretch A and MacManus DG. Surrogate model of compex non-linear data for preliminary nacelle design. *Aerospace Science and Technology*, Vol. 84, pp 399-411, 2019.

[12] Giangaspero G, MacManus D and Goulos I. Surrogate models for the prediction of the aerodynamic performance of exhaust systems. *Aerospace Science and Technology*, Vol. 92, pp 77-90, 2019.

[13] Giannakoglou KC, Papadimitriou DI and Kampolis IC. Aerodynamic shape design using evolutionary algorithms and new gradient-assisted metamodels. *Computer Methods in Applied Mechanics and Engineering*, Vol. 195, pp 6312-6329, 2006.

[14] Wang Q and Zhao Q. Rotor blade aerodynamic shape optimization based on high-efficient optimization method. *Proceedings of the Institution of Mechanical Engineers, Part G: Journal of Aerospace Engineering*, Vol. 234, No. 2, pp 375-387, 2019.
[15] Lindhorst K, Haupt MC and Horst P. Efficient surrogate modelling of nonlinear aerodynamics in aerostructural coupling schemes. *AIAA Journal*, Vol. 52, No. 9, pp 1952-1966, 2014.
[16] Thuerey N, Weißenow K, Prantl L and Hu X. Deep learning methods for reynolds-averaged navier-stokes simulations of airfoil flows. *AIAA Journal*, Vol. 58, No. 1, pp 25-36, 2020.
[17] Zuccolo G, Christie R, MacManus D, Goulos I and Martin P. Low order models for transonic afterbody aerodynamic characteristics. *AIAA SciTech Forum*, Orlando, USA, 6-10 January 2020, AIAA2020-1997.
[18] Tejero F, MacManus D, Hueso-Rebassa J, Sanchez-Moreno F, Goulos I and Sheaf C. Aerodynamic optimisation of civil aero-engine nacelles by dimensionality reduction and multi-fidelity techniques. *56th 3AF International Conference*, Toulouse, France, 28-30 March 2022.
[19] Rossow CC, Godard JL, Hoheisel H and Schmitt V. Investigation of propulsion integration interference effects on a transport aircraft configuration. *Journal of Aircraft*, Vol. 31, pp 1022-1030, 1994.
[20] Koc S, Kim H and Nakahashi K. Aerodynamic design of wing-body-nacelle-pylon configuration. *17th AIAA Computational Fluid Dynamics Conference*, Toronto, Canada, 6-9 June 2005, AIAA2005-4856.
[21] Schreiner BDJ, Tejero F, MacManus DG and Sheaf C. Robust aerodynamic design of nacelles for future civil aero-engines. *Proceedings of ASME Turbo Expo*, virtual, 21-25 September 2020, GT2020-14470.
[22] FAA. Title 14, Chapter 1, Subchapter C, Part 33 – Airworthiness standards: aircraft engines, Subpart G. Authority report, FAA-2002-6717, 2007.
[23] Christie R, Heidebrecht A and MacManus D. An automated approach to nacelle parameterization using intuitive class shape transformation curves. *Journal of Engineering for Gas Turbines and Power*, Vol 139, pp 1-9, 2017.
[24] Tejero F, MacManus DG and Sheaf C. Impact of droop and scarf on the aerodynamic performance of compact aero-engine nacelles. *AIAA SciTech Forum*, Orlando, USA, 6-10 January 2020, AIAA2020-1522.
[25] Tejero F, Christie R, MacManus D and Sheaf C. Non-axisymmetric aero-engine nacelle design by surrogate-based methods. *Aerospace Science and Technology*, Vol. 117, 106890,2021.
[26] Christie R, Robinson M, Tejero F and MacManus DG. The use of hybrid intuitive class shape transformation curves in aerodynamic design. *Aerospace Science and Technology*, Vol. 95, 105473, 2019.
[27] Goulos I, Stankowski T, Otter J, MacManus D, Grech N and Seaf C. Aerodynamic design of separate-jet exhausts for future civil aero-engines – Part I: parametric geometry definition and computational fluid dynamics approach. *Journal of Engineering for Gas Turbines and Power*, Vol. 138, No. 8, pp 1-14, 2016.
[28] Goulos I, Otter J, Tejero F, Hueso-Rebassa J, MacManus D and Sheaf C. Civil turbofan propulsion aerodynamics: thrust-drag accounting and impact of engine installation position. *Aerospace Science and Technology*, Vol. 111, pp 1-14, 2021.
[29] Rivers MB and Dittberner A. Experimental investigation of the NASA common research model. *Journal of Aircraft*, Vol. 51, No. 4, pp 1183-1193, 2014.
[30] Ansys Inc. 275 Technology Drive, Canonsburg, Pa 15317, ANSYS FLUENT User's Guide.
[31] Menter FT. Two-equations eddy-viscosity turbulence models for engineering applications. *AIAA journal*, Vol. 32, No. 8, pp 1598-1605, 1994.
[32] Vassberg JC, Tinoco EN, Mani M, Rider B, Zickuhr T, Levy DW, Brodersen OP, Eisfeld B, Crippa S, Wahls RA, Morrison JH, Mavriplis DJ and Murayama M. Summary of the fourth AIAA computational fluid dynamics drag prediction workshop. *Journal of Aircraft*, Vol. 51, No. 4, pp 1070-1089, 2014.
[33] M.I.D.A.P.M.S. Group. Guide to in-flight thrust measurement of turbojets and fan engines. Report AG-237, AGARDograp, 1979.
[34] Forrester AIJ, Sbester A and Keane AJ. *Engineering design via surrogate modelling: a practical guide*. Wiley, 2008.
[35] Dongare AD, Kharde RR and Kachare AD. Introduction to artificial neural network. *International Journal of Engineering and Innovative Technology*, Vol. 2, No. 1, pp 189-194, 2012.
[36] Shanmuganathan S and Samarasinghe S. *Artificial neural network modelling*. Springer, 2016.
[37] Buscema M. Back propagation neural networks. *Substance Use and Misuse*, Vol. 33, No. 2, pp 233-270, 1998.
[38] Kingma DP and Ba J. Adam: a method for stochastic optimization. *3rd International Conference on Learning Representation*, San Diego, USA, 7-9 May 2015.